Biophysical Journal, Volume *120*

Supplemental information

Quantifying viscosity and surface tension of multicomponent protein-nucleic acid condensates

Ibraheem Alshareedah, George M. Thurston, and Priya R. Banerjee

Materials and Methods

Peptide and DNA sample preparation: The peptide ($[RGRGG]_5$) was purchased from Genscript USA Inc. (NJ, USA) and contains a C-terminal cysteine for site-specific peptide labeling. Peptide stock solutions were prepared in RNase-free water (Santa Cruz Biotechnology) with 50 mM dithiothreitol (DTT). Custom-synthesized DNA oligos, poly(dT)-T40 [40 nucleobases; molecular weight =12106 Da] and Atto488 labeled (5')-dT40 were purchased from Integrated DNA Technologies (IDT). The DNAs were reconstituted in RNase-free water. The concentration of DNA stocks was calculated from their respective measured absorbance at 260 nm in a UV-Vis spectrophotometer (Nanodrop oneC). Both DNA and peptide stock solutions were stored at −20 °C. All peptide-DNA condensates were prepared in a buffer containing 25 mM Tris-HCl (pH 7.5), 25 mM NaCl and 20 mM DTT unless otherwise noted. The peptide concentration was kept at 5.0 mg/ml (~2 mM) throughout this study and the DNA concentration was varied as indicated.

All concentrations in this paper are reported in [nucleotide]:[Arg] molar ratios.

Fluorescence labeling: The RGRGG repeat peptide contains a C-terminal cysteine which was used for site-specific labeling with Alexa594 dyes using the same protocol (Cys-maleimide chemistry) as described in our earlier work[1-5]. The labeling efficiency for the peptide samples was observed to be ≥ 90% (UV-Vis absorption measurements).

Fusion of suspended droplets using optical traps: Optical trap mediated droplet fusion assays were conducted to investigate the inverse capillary velocity of DNA-peptide condensates, as previously described[6]. Briefly, samples containing DNA-peptide condensates at the indicated [T]/[Arg] ratios were injected into a tween 20-coated (20% v/v) 25 mm x 75 mm x 0.1 mm flow chamber (custom-made). Condensates were trapped using a dual-trap optical tweezer system that also offers laser scanning confocal fluorescence microscopy (LUMICKS™, C-trap). Droplets were independently trapped far from each other in two optical traps (using a 1064 nm laser) and then brought into proximity. The 2nd trap was held at a fixed position while the 1st trap was programmed to move at a constant speed of 40-100 nm/s in the direction of the 2nd trap. Coalescence started upon contact due to interfacial tension. The motion of the 1st trap was stopped when the fused droplet relaxed to a spherical shape. The force-time signal was recorded at a 78.2 kHz sampling frequency (i.e., ~13 μs time interval) and analyzed using the following fusion relaxation model[7]:

$$F = ae^{(-t/\tau)} + bt + c \quad (1)$$

where the parameter τ is the fusion relaxation time. The 2nd term in equation (1) accounts for the constant velocity of the 1st trap. ~ 10-20 fusion events were recorded for each sample, then and the corresponding relaxation time was plotted as a function of the average diameter (as determined by fluorescence images before fusion) of the fusing droplets and fitted using a linear model of inverse capillary velocity[8].

Video Particle Tracking (VPT) Microscopy: Samples were prepared by mixing the polypeptide and the ssDNA in a buffer containing fluorescent beads (0.0003% solids, 200 nm carboxylate-coated yellow-green polystyrene spheres; FluoSpheres™, Invitrogen). Upon condensate formation, beads were found to be embedded in the condensates (see Fig. 1c, main text). Next, samples were placed on a tween 20-coated (20% v/v) microscope coverslip and sandwiched with a 1 mm thick microscope glass slide as described in our earlier work[8]. Following that, oil was injected into the chamber to prevent evaporation-induced hydrodynamic currents within the sample. After sealing with oil, samples were left to equilibrate for 0.5-2 hours or until all droplets have settled on the glass surface. Samples were then imaged using an epifluorescence microscope (Zeiss Primovert inverted iLED microscope with a 100× oil-immersion objective lens

and a Zeiss Axiocam 503 monochrome camera). Movies capturing the Brownian motion of the fluorescent beads within peptide-DNA condensates were collected at variable acquisition rates to ensure that the measured viscosity is independent of the acquisition rate of the microscope[9]. For each peptide-DNA mixing ratio, three independent samples were made on different days, 2-4 movies/per sample were collected imaging a total of 5-10 condensates, each condensate contained 10-100 microspheres. Particle tracking was done using the open-source particle tracking software TrackMate[10] (v6.0.1). Tracking results were also cross-validated using TrackPy python-based particle tracking library (v0.4.2)[11]. Trajectories were corrected for sample-stage drift and then the mean squared displacement (MSD) was calculated for each trajectory using a custom-built python script as a function of the lag time (τ). To eliminate any effects coming from the interface of the condensate with the surrounding dilute phase, trajectories of particles that are proximal to the interface were discarded. The ensemble-averaged MSD was obtained and fitted using the following equation

$$MSD(\tau) = < r^2 > (\tau) = 4D\tau^{\alpha} \quad (2)$$

Where D is the diffusion coefficient of the bead and α is the diffusive exponent. For classical Brownian motion in a purely viscous fluid, the value of α is equal to unity. α values for all the condensates tested were in the range of 0.9-1.2. The viscosity η of the condensate is then determined using the Stokes-Einstein equation ($\eta = \frac{k_B T}{6\pi D R}$), where D = diffusion coefficient, k_B = Boltzmann constant, η = viscosity of the medium, R is the radius of the bead, T is the temperature.

Partition coefficient measurements: Images for partition analysis were collected using a Zeiss LSM710 laser scanning confocal microscope with a 63x oil-immersion objective (Plan-Apochromat 63x/1.4 oil DIC M27). The same samples were used for DNA-peptide mixtures as described in the droplet fusion section. All the confocal images were collected within 30 minutes of sample preparation. The partition coefficient (k) was calculated by dividing the mean intensity of Atto488-labeled dT40 or Alexa494-labeled RGRGG repeat polypeptide per unit area inside the droplet by the mean intensity per unit area in the external dilute phase ($k = \frac{I_{in}}{I_{out}}$). For each sample, 30-40 droplets were analyzed.

Turbidity measurements: $[RGRGG]_5$ and dT_{40} mixtures were prepared at a fixed peptide concentration (5 mg/ml) and variable ssDNA concentrations. Sample absorbance at 350 nm was measured using a spectrophotometer (Nanodrop oneC UV-Vis) with an optical path length of 1 mm. Each sample was prepared independently and measured. A similar protocol was followed for recording turbidity of DNA-peptide mixtures at a fixed concentration and composition with variable [NaCl]. For each data point, two independently prepared samples were measured twice.

Fluorescence correlation spectroscopy: Samples containing 10-100 pM bulk concentration of either Atto488-labeled dT40 or Alexa594-labeled $[RGRGG]_5$ were injected into a tween 20-coated 25 mm x 75 mm x 0.1 mm custom-made flow chamber and loaded onto the microscope stage (Lumicks, C-trap) equipped with a single-photon avalanche photodiode (sAPD). We varied the labeled species concentrations such that their concentrations within the condensates are suitable for FCS measurements, which was judged by the signal to noise ratio of the autocorrelation curves. The optimal location for collecting FCS intensity-time traces was selected by first collecting a point Z-scan at the center of the condensate. The location with maximal intensity was identified and measurements of the photon arrival times were acquired at a 72.8 kHz sampling rate by performing a point scan at the center of the peptide-DNA condensate at the optimal location (**Fig. S10**). The excitation power was kept at a minimum to avoid photobleaching of the fluorophores. Each point scan was collected over 5 minutes. For each sample, five point-scans from different condensates were obtained and analyzed as follows. For each point scan, the

autocorrelation function was calculated for different lag times using the multipletau (v0.1.9) and pycorrelate (v0.2.1) python libraries[12,13]. The Autocorrelation function was fitted with the following equation

$$G(\tau) = G_0 \left(1 + \frac{4D\tau}{\omega^2}\right)^{-1} \left(1 + \frac{4D\tau}{\omega_z^2}\right)^{-\frac{1}{2}} + G_{inf} \quad (3)$$

here, D is the diffusion coefficient of the fluorescent probe and ω, ω_z are the radial and axial dimensions of the confocal volume, respectively, under the three-dimensional Gaussian approximation[14]. In the fitting process, the structural parameters ω and ω_z were fixed to the values obtained from the calibration procedure described below and only G_0, D and G_{inf} were allowed to vary. The diffusion coefficient was extracted from the fit for each autocorrelation curve. The diffusion coefficient values were averaged and their standard deviation was taken as the uncertainty. A similar procedure was used for measuring the diffusion of 20 nm beads in glycerol/water mixtures except that the FCS intensity-time traces were collected from random points on the XY plane that is approximately at the middle between the lower and upper surfaces of the sample chamber (about 40 μm above the lower glass surface).

For calibration, we used a combination of free dye molecules as well as fluorescent beads. Briefly, we used Alexa488 dye and Alexa594 to calibrate the lasers by collecting FCS intensity-time series and calculating autocorrelation curves (**Fig. S11**). Then, by fixing the diffusion coefficient D to the known diffusion coefficients of the probes, we performed the fittings to determine the structural parameters of the confocal volume. We also confirmed confocal volume measurements by performing FCS calibration on 20 nm and 200 nm polystyrene beads (FluoSpheres™, Invitrogen) in water and found that the confocal volume structural parameters lie within the acceptable range (producing D values of 22.4 μm^2/s and 0.8 μm^2/s, respectively). The diffusion coefficient values for these two bead types in water at 24 °C (the temperature of our microscope chamber) as calculated from the Stokes-Einstein equation are 24.45 and 2.445 μm^2/s, respectively. The value for the 20 nm beads was closer to the accepted values and therefore, 20 nm beads were used to estimate the viscosity of glycerol-water mixtures. The combined calibration procedures yielded a beam waist of 320 ± 20 nm for the green laser line and 340± 20 nm for the red laser line. The beam axial dimension was fluctuating between 2-10 μm. We note that the diffusion-based calibration is not accurate for determining the axial dimension of the confocal volume due to the sensitivity of the correlation plateau to the probe concentration[15]. Nevertheless, the axial dimension is unlikely to contribute to the extracted values of the diffusion coefficient and does not alter the shape of the autocorrelation function[15].

Data processing software: Excel 2016 was used for partition calculations. All numerical/statistical analysis was done in custom-built Python procedures. Fiji-ImageJ[16] (version 1.52p) was used for image processing. OriginPro (2018b) was used for Graphing. Adobe Illustrator CC (2019) was used for the figure assembly and production.

Theoretical Phase Diagram: The liquid-liquid phase separation spinodal, tie lines, and critical points were computed with the use of a Flory-Huggins mixture model with two polymers in a solvent.

$$\frac{F}{k_B T} = \frac{\varphi_1 \ln(\varphi_1)}{\gamma_1} + \frac{\varphi_2 \ln(\varphi_2)}{\gamma_2} + w_{11}\varphi_1^2 + w_{12}\varphi_1\varphi_2 + w_{22}\varphi_2^2 + (\varphi_1 + \varphi_2) + (1 - \varphi_1 - \varphi_2)\ln(1 - \varphi_1 - \varphi_2)$$

Here, the ϕ's are volume fractions, the γ's are size parameters, and the w's are mean-field interaction parameters. The parameters used for the computation of the representative closed-loop boundary were γ_1 = 300, γ_2 = 7000, w_{11} = 1.0, w_{22} = -0.35, and w_{12} = -2.15.

The computation of the closed-loop phase boundaries, spinodal, and critical points, coded in Mathematica, first searches along rays in composition space through the origin, for points at which the least eigenvalue of the Hessian matrix of the free energy taken with respect to the two volume fractions first changes sign from positive to negative. Then, by making small steps in directions orthogonal to the composition-gradient of the determinant of the Hessian, while at the same time correcting periodically to ensure that the full determinant of the Hessian remains zero, a closely spaced series of points is generated along the spinodal. To locate the critical points while stepping along the spinodal, the algorithm also searches for and refines any points on the spinodal at which the directional derivative of the spinodal curve becomes parallel to that eigenvector of the Hessian that belongs to its least eigenvalue.

The method used here for computing the tie lines takes advantage of the fact that the collection of tie lines corresponds to the self-intersections of the mapping of the composition triangle into the space of the three chemical potentials. The mapping is that created by the ternary free energy of mixing, a model in the present case. Because linear terms in the free energy of mixing do not influence the thermodynamic conditions for liquid-liquid phase separation, for numerical work it can be convenient to remove them in advance, as was done for the expression given above, in view of the Taylor expansion of the logarithmic term.

Starting tie lines were located by first identifying a composition point entirely inside the spinodal, evaluating the difference between the chemical potentials of the two solute components at that point, then creating a curve in composition space for which this difference remained the same. The algorithm then maps small segments along this curve into the space of the chemical potentials of the solvent and of component 1, and searches for intersections of the images of those segments in that chemical potential space. Approximate intersections so found are then refined to provide good starting tie lines, by demanding that each chemical potential is the same at each composition endpoint. For numerical work, it was found sometimes helpful to use the logarithms of the volume fractions, due to the low volume fractions that can occur along the coexistence curve.

Finally, having located such a starting, refined tie line, the algorithm makes small steps that remain close to the self-intersections of the chemical potential mapping, then refines each step to continue to require equality of all three chemical potentials. In order to make the small steps in good directions, it is helpful to recognize that directions that will locally follow a collection of tie lines can be written as a generalized cross product of the gradient vectors of each chemical potential, each such vector being a function of the four coordinates that combine the compositions of the two endpoints. An analogous method can be used for following the contours of any differentiable map from R^n to R^{n-1}, closely related to more general methods[17] that inspired the present one[18].

Supplementary Figures

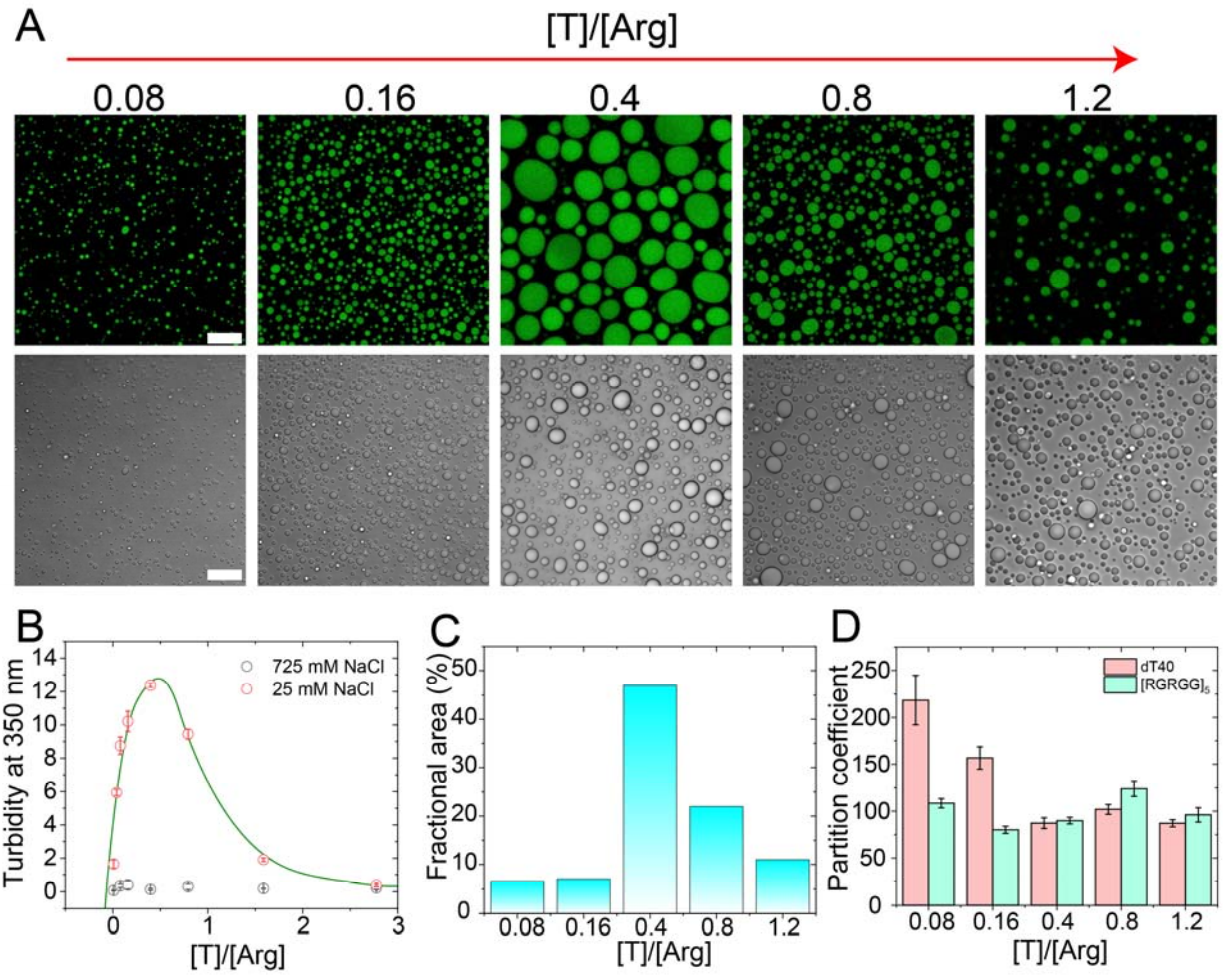

Fig. S1. Condensation of $[RGRGG]_5$-dT40 mixtures at different [T]/[Arg] ratios. (A) Fluorescence and bright-field images of $[RGRGG]_5$-dT40 condensates. Scale bars represent 20 μm. **(B)** Turbidity at 350 nm as a function of increasing [T]/[Arg] ratio at 25 mM and 725 mM salt concentrations. The green line is drawn as a guide to the eye. The incubation time for this measurement is 2-3 minutes after vigorous mixing. **(C)** Fractional area of the condensed phase as calculated from Fiji-ImageJ software as a function of [T]/[Arg] ratio. **(D)** Partition coefficient of dT40 and $[RGRGG]_5$ as a function of [T]/[Arg] ratio.

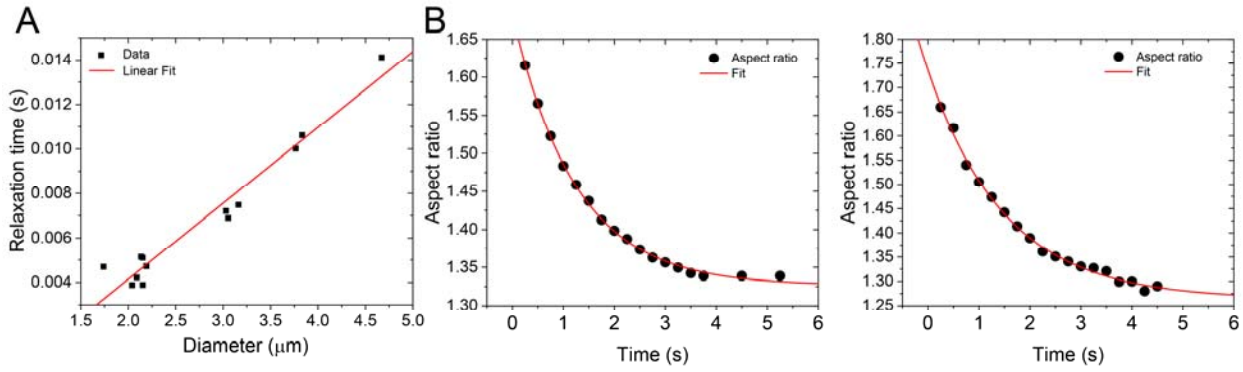

Fig. S2. Determination of inverse capillary velocity: (A) Active fusion: Linear relation between the fusion-relaxation time and the diameter of the condensates for the active fusion of suspended droplets using a dual-trap optical tweezer. The relaxation time is obtained from the laser signal as trapped condensates undergo fusion (see Fig. 1B in the Main-text). The slope of the linear fit represents the scaled relaxation time which is proportional to the ratio of η/γ (see Equation-1, Main-text). **(B) Passive fusion:** Aspect ratio analysis of two instances of passive fusion of two condensates on a tween-coated glass coverslip surface (see Movies S1 and S2). These condensates were prepared identically as in Fig. S2A for our active fusion assay. The exponential fits give a normalized relaxation time of ~100 ms/μm, which is more than one order of magnitude higher than the same obtained from OTF experiments (~3.4 ms/μm). These data indicate a dominant role of surface drag force during passive droplet fusion on a microscope coverslip for these condensates.

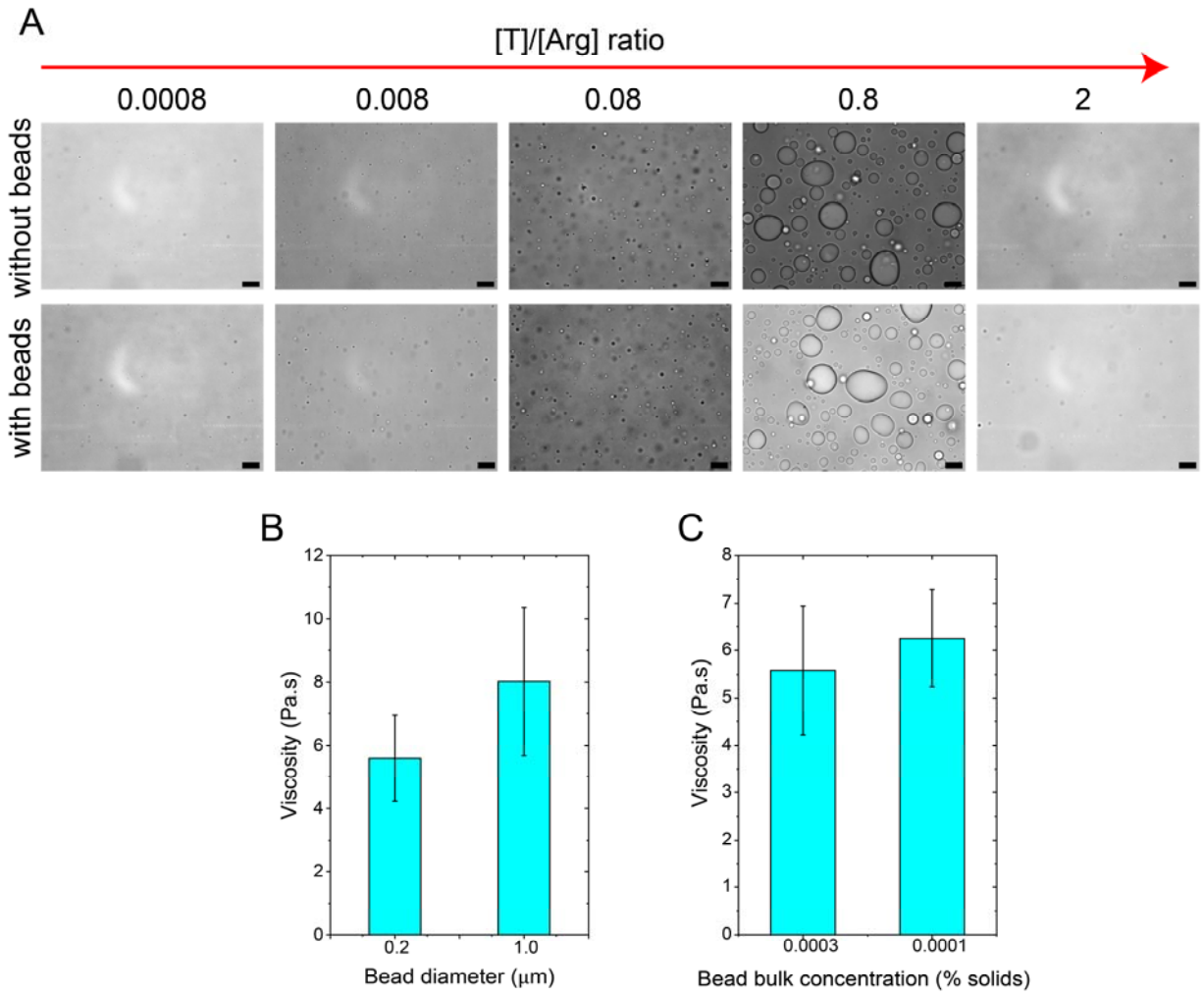

Fig. S3. (A) Bright-field microscopy images for $[RGRGG]_5$-dT40 condensates in the presence and absence of beads. Scale bar represents 10 μm. **(B)** Viscosity of $[RGRGG]_5$-dT40 condensates prepared at [Arg]/[T]=0.4 as determined by particle tracking of two bead diameters; 0.2 and 1.0 μm. **(C)** Viscosity of $[RGRGG]_5$-dT40 condensates prepared at [Arg]/[T]=0.4 for different bead concentrations.

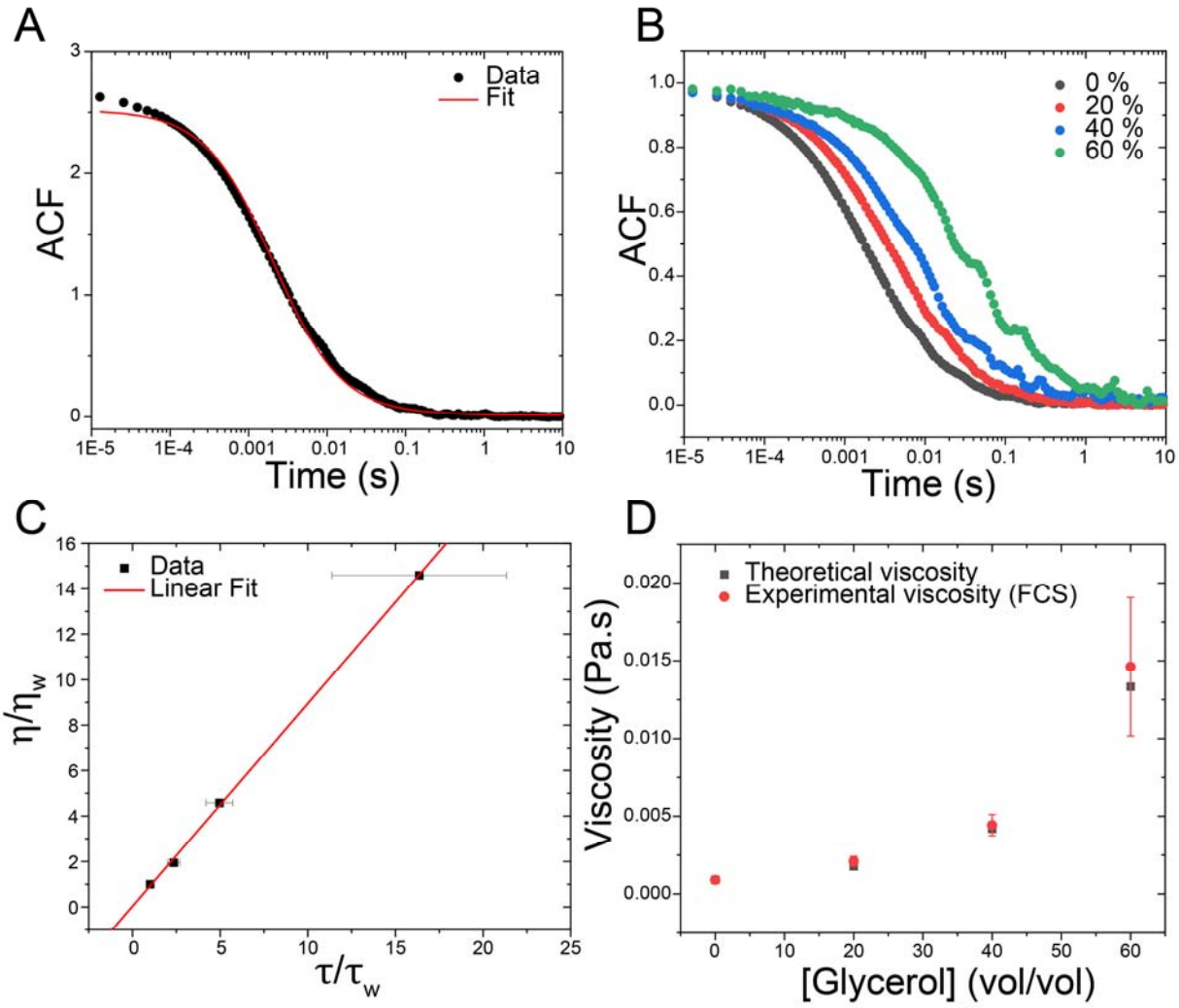

Fig. S4. Diffusion of 20 nm beads in glycerol/water mixtures as measured by FCS. (A) Autocorrelation function and fit for 20 nm bead diffusion in water. **(B)** Autocorrelation functions of the same beads in glycerol/water mixtures. **(C)** Viscosity and diffusion time normalized by their respective values in water showing a linear correlation, consistent with what was previously found in Sherman et al[19]. **(D)** Measured viscosity calculated from the Stoke-Einstein equation and the FCS-derived diffusion coefficient overlaid on the expected viscosity of glycerol/water mixtures as calculated by the formula reported in the literature[20,21], which were also compared with published experimental results[22].

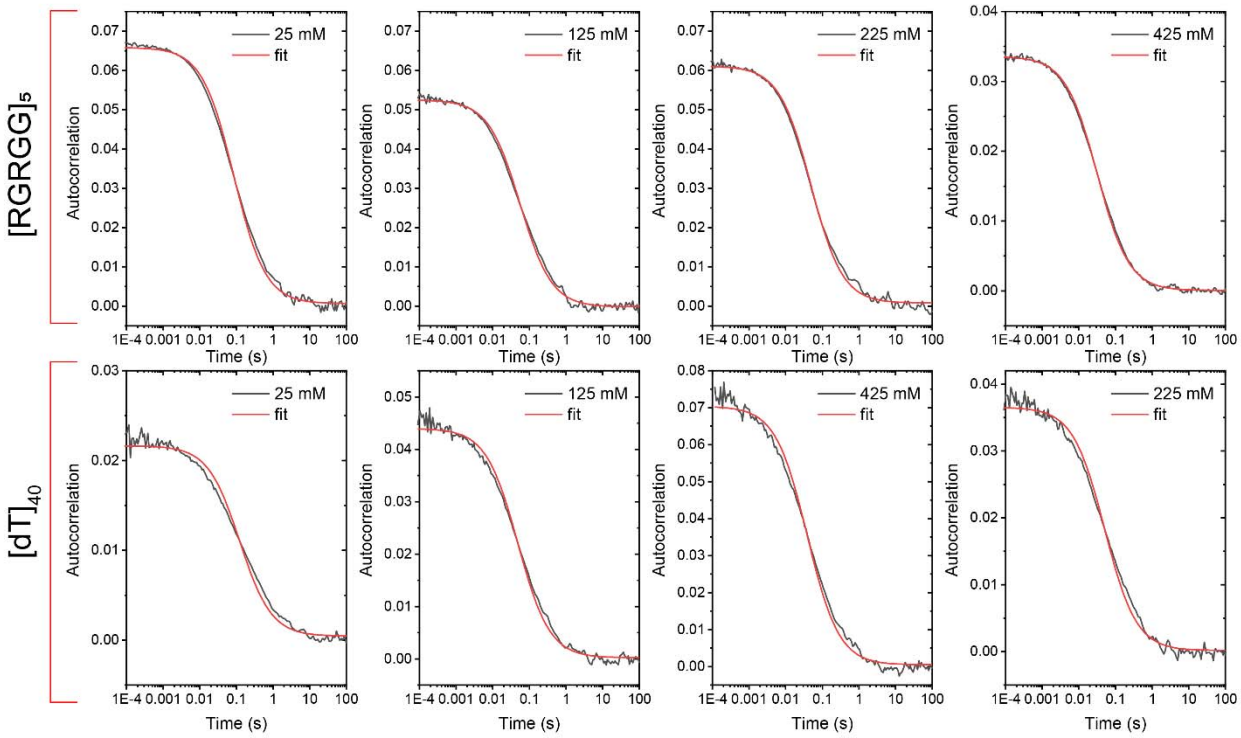

Fig. S5. Representative FCS autocorrelation curves for Atto488-dT40 and Alexa594-$[RGRGG]_5$ within $[RGRGG]_5$-dT40 condensates at various salt (NaCl) concentrations. The top row corresponds to the autocorrelation curves for Alexa594-$[RGRGG]_5$ diffusion within the condensates. The bottom row corresponds to the autocorrelation curves for Atto488-dT40 diffusion within the condensates. The red lines are fits of Equation-3 (see *Fluorescence correlation spectroscopy* section in Methods).

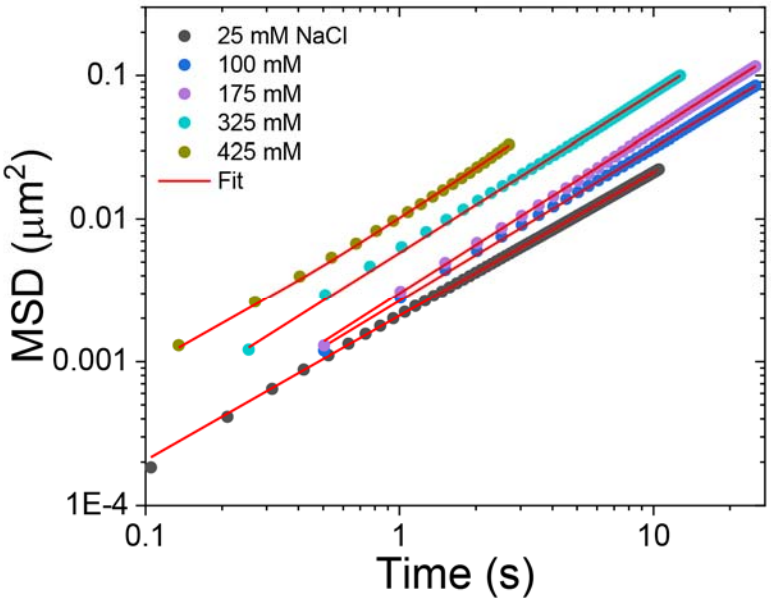

Fig. S6. Ensemble-averaged mean squared displacement (MSD) as a function of increasing salt concentration for 200 nm beads within $[RGRGG]_5$-dT40 condensates prepared at a ratio of [T]/[Arg] = 0.40. The red lines are fits of Equation-2 added to a constant (See *video particle tracking microscopy* section in Methods).

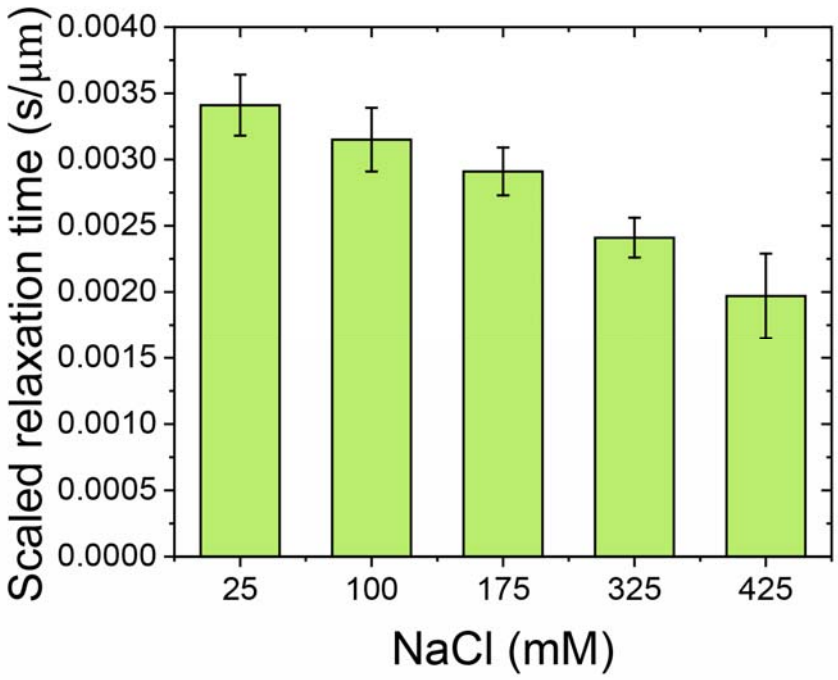

Fig. S7. Scaled fusion relaxation time for $[RGRGG]_5$-dT40 condensates, prepared at various salt concentrations, using our OTF assay.

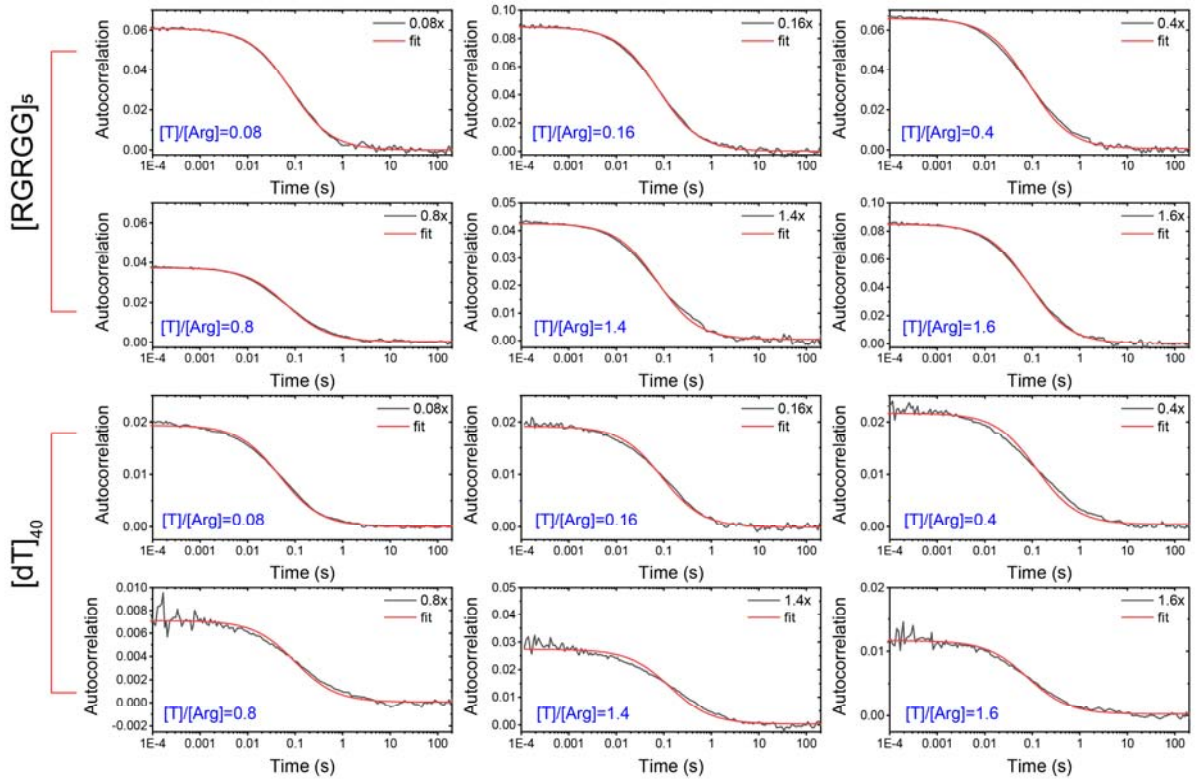

Fig. S8. Representative FCS autocorrelation curves for Atto488-dT40 and Alexa594-[RGRGG]$_5$ within [RGRGG]$_5$-dT40 condensates at various mixing ratios. The top two rows correspond to the autocorrelation curves of Alexa594-[RGRGG]$_5$ within these condensates. The bottom two rows show autocorrelation curves for Atto488-dT40 within these condensates. The red lines are fits of Equation-3 (see *Fluorescence correlation spectroscopy* section in Methods).

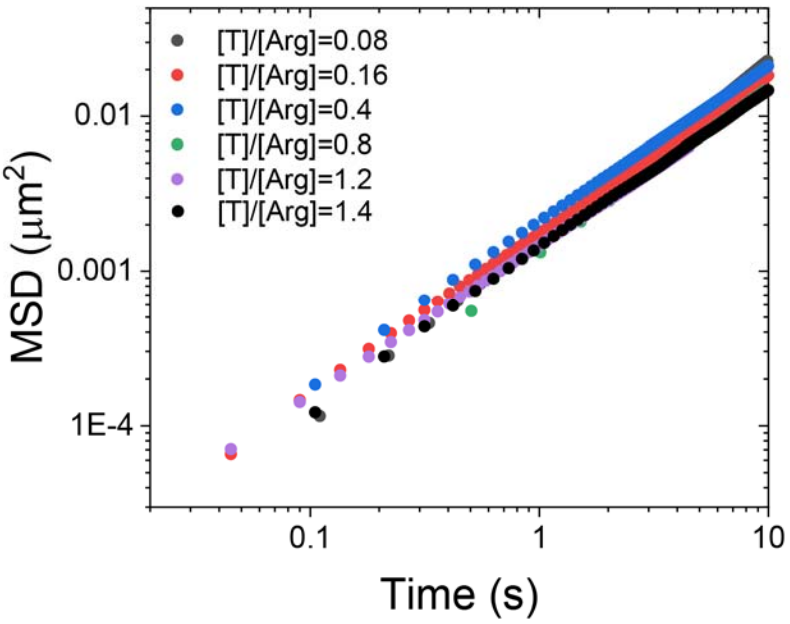

Fig. S9. Ensemble-averaged mean squared displacements (MSD) of 200 nm beads within $[RGRGG]_5$-dT40 condensates at variable [T]/[Arg] mixing ratios as indicated.

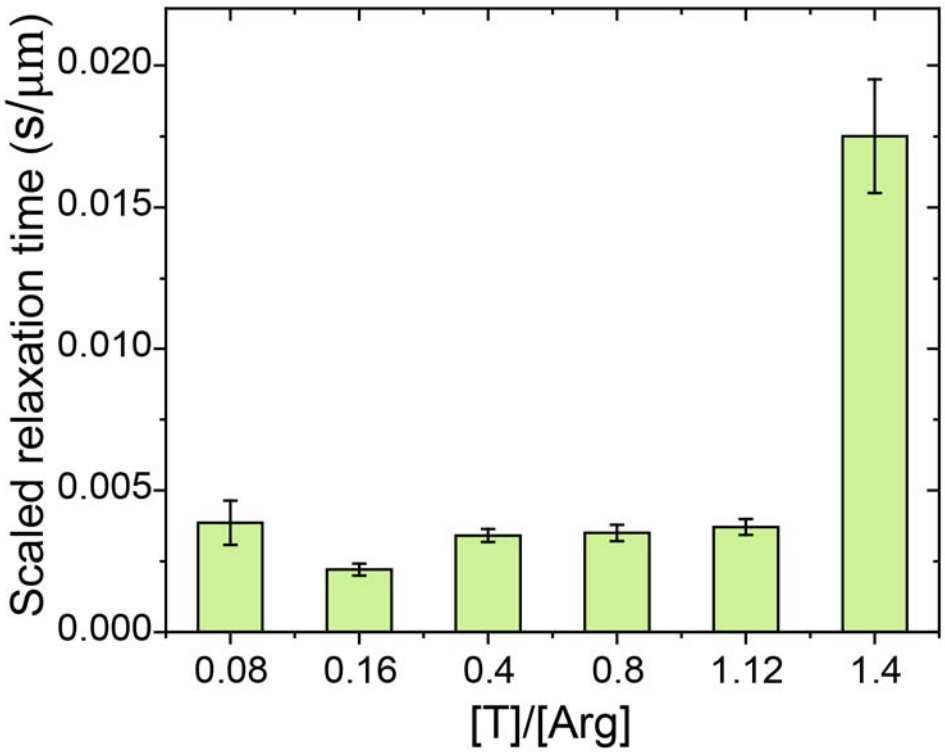

Fig. S10. Scaled fusion relaxation time of $[RGRGG]_5$-dT40 condensates, prepared at different [T]/[Arg] molar ratios, from our OTF assay. For higher [T]/[Arg] ratios (*e.g.* [T]:[Arg] = 1.6), we observed that droplets do not fuse (see Movies S3&S4 and Figure 3E in the Main-text).

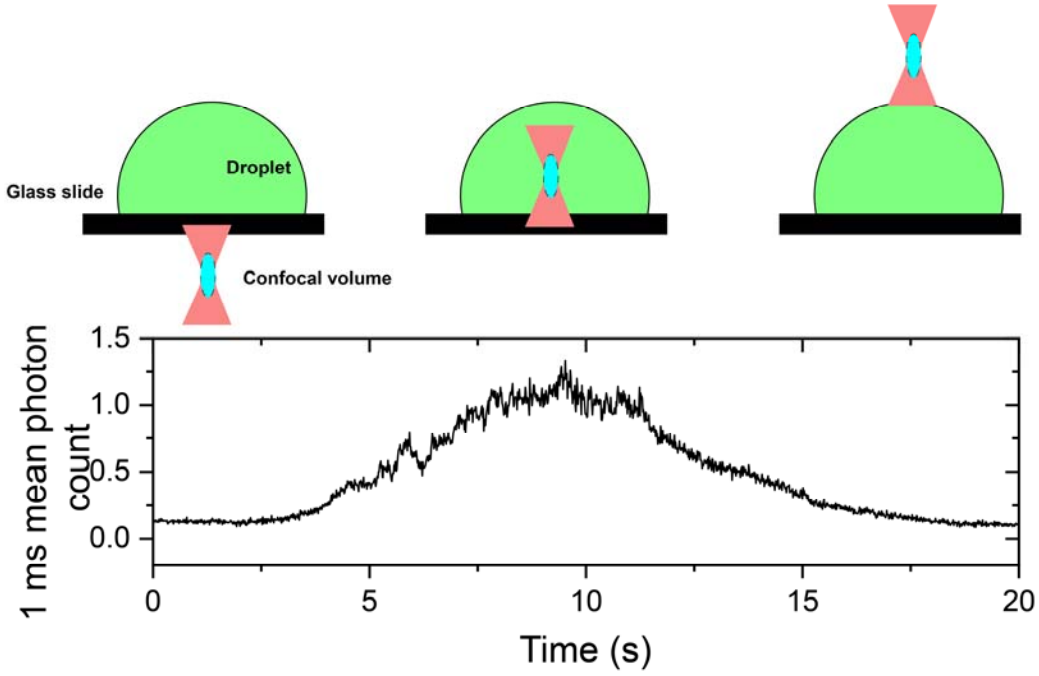

Fig. S11. Point Z-scan at the center of a $[RGRGG]_5$-dT40 condensate. The confocal volume is initially placed on the glass slide surface where only photons from the background are detected. The nanostage of the microscope was then set to move in the Z-direction in steps of 200 nm and three steps per second. The Z-location of the nanostage that corresponds to the maximum intensity is chosen for FCS measurements. Condensates that were large enough (~ 15 μm in diameter) were considered for FCS measurements. This is to ensure that the location of the confocal volume is ≥ 6 μm above the glass surface.

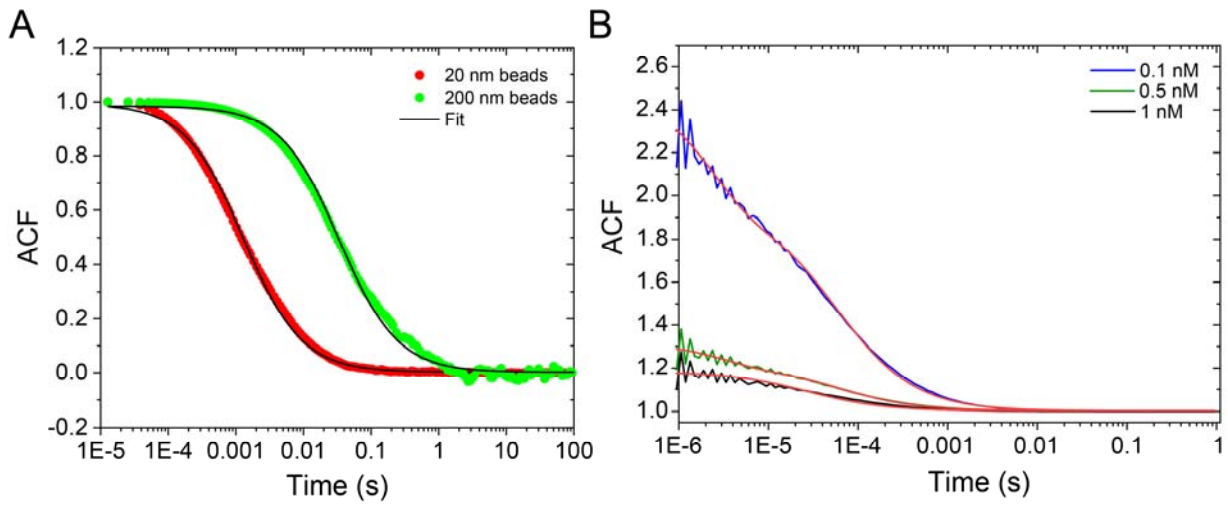

Fig. S12. (A) Autocorrelation curves for the diffusion of 20 nm beads and 200 nm beads in water as measured by FCS. **(B)** Autocorrelation and fits for the diffusion of free Alexa-488 dye in water. The fits in **(B)** are using Equation-3 with a triplet state term[23]. The fits in **(A)** are using Equation-3 (see *Fluorescence correlation spectroscopy* section in Methods).

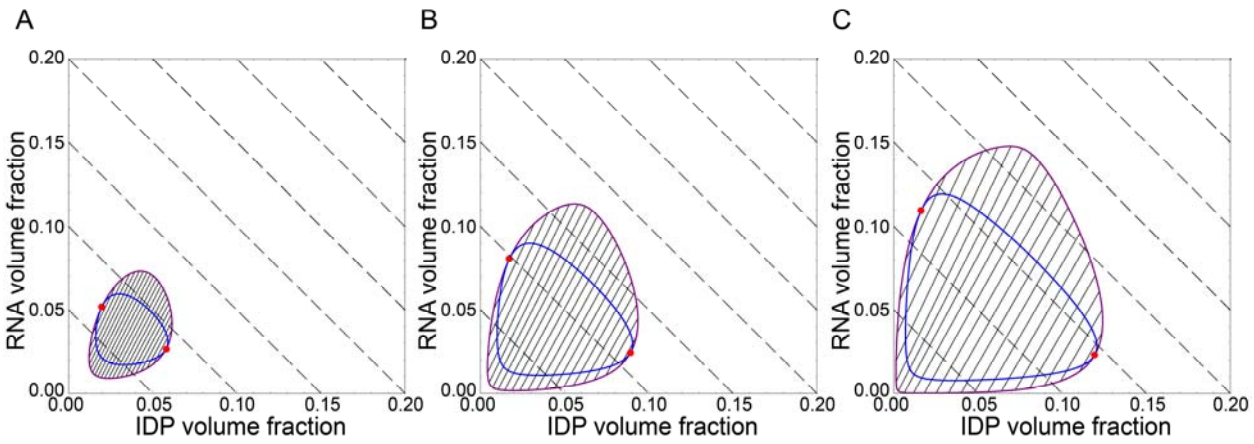

Fig. S13. Computed model phase diagrams showing that the extent of the calculated closed-loop two-phase regime is sensitive to increasing NA-IDP attraction strength**.** Parameters used were γ_1 = 100, γ_2 = 370, w_{11} = 0.4, w_{22} = -0.3 for all panels, while in **(A)** w_{12} = -2.2, **(B)** w_{12} = -2.27, **(C)** w_{12} = -2.35. [IDP: Intrinsically disordered polypeptide].

Supporting References

1 Alshareedah, I. *et al.* Interplay between Short-Range Attraction and Long-Range Repulsion Controls Reentrant Liquid Condensation of Ribonucleoprotein–RNA Complexes. *Journal of the American Chemical Society* **141**, 14593-14602, doi:10.1021/jacs.9b03689 (2019).

2 Banerjee, P. R., Moosa, M. M. & Deniz, A. A. Two-Dimensional Crowding Uncovers a Hidden Conformation of α-Synuclein. *Angewandte Chemie* **128**, 12981-12984 (2016).

3 Banerjee, P. R. & Deniz, A. A. Shedding light on protein folding landscapes by single-molecule fluorescence. *Chemical Society Reviews* **43**, 1172-1188 (2014).

4 Banerjee, P. R., Milin, A. N., Moosa, M. M., Onuchic, P. L. & Deniz, A. A. Reentrant Phase Transition Drives Dynamic Substructure Formation in Ribonucleoprotein Droplets. *Angew Chem Int Ed Engl* **56**, 11354-11359, doi:10.1002/anie.201703191 (2017).

5 Banerjee, P. R., Mitrea, D. M., Kriwacki, R. W. & Deniz, A. A. Asymmetric Modulation of Protein Order-Disorder Transitions by Phosphorylation and Partner Binding. *Angew Chem Int Ed Engl* **55**, 1675-1679, doi:10.1002/anie.201507728 (2016).

6 Kaur, T. *et al.* Molecular Crowding Tunes Material States of Ribonucleoprotein Condensates. **9**, 71 (2019).

7 Patel, A. *et al.* A Liquid-to-Solid Phase Transition of the ALS Protein FUS Accelerated by Disease Mutation. *Cell* **162**, 1066-1077, doi:https://doi.org/10.1016/j.cell.2015.07.047 (2015).

8 Alshareedah, I., Kaur, T. & Banerjee, P. R. in *Methods in Enzymology* (Academic Press, 2020).

9 McGlynn, J. A., Wu, N. & Schultz, K. M. Multiple particle tracking microrheological characterization: Fundamentals, emerging techniques and applications. *Journal of Applied Physics* **127**, 201101 (2020).

10 Tinevez, J.-Y. *et al.* TrackMate: An open and extensible platform for single-particle tracking. *Methods* **115**, 80-90 (2017).

11 Allan, D. et al., DOI: 10.5281/zendo.60550 (2019).

12 Paul Müller (2012) *Python multiple-tau algorithm* (Version 0.1.9). Available at https://pypi.python.org/pypi/multipletau/ (Accessed 15 Sep 2020).

13 see pycorrelate documentation at https://pycorrelate.readthedocs.io/en/latest/.

14 Enderlein, J., Gregor, I., Patra, D., Dertinger, T. & Kaupp, U. B. Performance of fluorescence correlation spectroscopy for measuring diffusion and concentration. *ChemPhysChem* **6**, 2324-2336 (2005).

15 Rüttinger, S. *et al.* Comparison and accuracy of methods to determine the confocal volume for quantitative fluorescence correlation spectroscopy. *Journal of microscopy* **232**, 343-352 (2008).

16 Schindelin, J. *et al.* Fiji: an open-source platform for biological-image analysis. *Nature methods* **9**, 676 (2012).

17 Dobkin, D. P., Wilks, A. R., Levy, S. V. F. & Thurston, W. P. Contour tracing by piecewise linear approximations. *ACM Transactions on Graphics* **9**, 389–423, doi:10.1145/88560.88575 (1990).

18 W.P. Thurston, personal communication.

19 Sherman, E. *et al.* Using fluorescence correlation spectroscopy to study conformational changes in denatured proteins. *Biophysical journal* **94**, 4819-4827 (2008).

20 Cheng, N.-S. Formula for the viscosity of a glycerol− water mixture. *Industrial & engineering chemistry research* **47**, 3285-3288 (2008).

21 Volk, A. & Kähler, C. J. Density model for aqueous glycerol solutions. *Experiments in Fluids* **59**, 75 (2018).

22 Segur, J. B. & Oberstar, H. E. Viscosity of glycerol and its aqueous solutions. *Industrial & Engineering Chemistry* **43**, 2117-2120 (1951).
23 Widengren, J., Mets, U. & Rigler, R. Fluorescence correlation spectroscopy of triplet states in solution: a theoretical and experimental study. *The Journal of Physical Chemistry* **99**, 13368-13379 (1995).